NUKLEONIKA 2016;61(4):393–401
doi: 10.1515/nuka-2016-0065

ORIGINAL PAPER

DE GRUYTER
OPEN

Diagnostics of laser-produced plasmas

Dimitri Batani,
Alessio Morace,
Yohann Maheut,
Katarzyna Jakubowska,
Luca Volpe

Abstract. We present the general challenges of plasma diagnostics for laser-produced plasmas and give a few more detailed examples: spherically bent crystals for X-ray imaging, velocity interferometers (VISAR) for shock studies, and proton radiography.

Key words: laser-produced plasmas • inertial-confinement fusion (ICF) • X-ray imaging • VISAR

D. Batani✉, Y. Maheut
University Bordeaux, CEA, CNRS, CELIA
(Centre Laser Intense at Applications), UMR 5107,
F-33405 Talence, France,
Tel.: +33 5 4000 3753,
E-mail: batani@celia.u-bordeaux1.fr

A. Morace
ILE, Institute of Laser Engineering,
University of Osaka, Japan

K. Jakubowska
Institute of Plasma Physics and Laser Microfusion,
23 Hery Str., 01-497 Warsaw, Poland
and University Bordeaux, CEA, CNRS, CELIA
(Centre Laser Intense at Applications), UMR 5107,
F-33405 Talence, France

L. Volpe
Centro de Laseres Pulsados (CLPU), Salamanca,
Universidad de Salamanca (USAL), Salamanca, Spain

Received: 25 August 2015
Accepted: 9 October 2015

Introduction

Laser-produced plasmas are used for a variety of studies, relevant for both basic physics and applications, and are of course essential within the study of inertial confinement approach to nuclear fusion. Because of this large interest, a large variety of diagnostics have been developed and are routinely used to unveil the physical processes at work during plasma process and laser-plasma interaction.

Nevertheless, the diagnostics of laser-produced plasmas poses several challenges. First of all, laser-produced plasmas have a small volume and short duration. Typically, the size is comparable to the laser spot dimension (micrometer to millimeter) and the lifetime is also comparable to the laser pulse duration (after the end of the laser pulse the plasma rapidly cools down and vanishes). Hence, diagnostics usually need to have high spatial and temporal resolution.

But indeed, the main challenge arises from the fact that the temperature and density of laser-produced plasmas span over several orders of magnitude and is characterized by the presence of very distinct plasma 'regions', which are all simultaneously present.

1) First, we have the 'undercritical region' (or plasma corona), which is defined by having a density smaller than the laser critical density, in practical units:

$$n_{cr}\ [\mathrm{cm}^{-3}] = 1.1 \times 10^{21} / \lambda^2\ [\mu\mathrm{m}] \quad (1)$$

This is a region in which the density decreases (because of plasma expansion) going away from the solid surface. This is also the region that is directly heated by the laser, can propagate up to n_{cr}, and, therefore, reaches high temperatures: a few hundreds of electron-volts up to a few kiloelectron-volts.

2) Then we have the 'conduction region' or overcritical region. Here the plasma cannot propagate and the heat is transported inwards by electrons (or by extreme ultraviolet radiation (XUV) and soft X-ray radiation generated in the corona). From the value reached in the corona, here the temperature drops down to a few electron-volts. The electron density increases from the n_{cr} value up to a few times 10^{23} cm^{-3}, or even more.

3) Then we have the 'shocked material'. Plasma expansion produces, because of momentum conservation, a shock wave that travels inward and compresses the target. The generated pressure can be as high as a few megabars, and the compression heats the material up to a few electron-volts. On the other side, such compression is irreversible but adiabatic. There is no heat transport from the other plasma regions (unless hot electrons or hard X-rays are generated during laser-plasma interaction).

Finally, we have the unperturbed solid.

The differences, several orders of magnitude in density and temperature, simultaneously present implies the need for having diagnostics within very large dynamics and also the need to use different diagnostics approaches and tools simultaneously.

For instance, the plasma corona, where a probe laser beam can propagate, can be characterized by optical diagnostics: interferometry [1], shadowgraphy [2, 3], Faraday rotation [4], etc. Also this region is very hot and hence emits X-rays. Therefore, one can use X-ray spectroscopy [5–9]. Optical spectroscopy can be used to characterize the parametric instabilities taking place in laser-plasma interaction [10–12]. And, finally, one can use particle detection (charge collectors, Faraday's cups, etc.) [13].

The overcritical region is the main source of soft X-rays and XUV radiation because even if the temperature is on an average lower than that in the corona, the density is much larger and then there are more collision and more photon emission. Hence, one can use emission X-ray spectroscopy but also absorption X-ray spectroscopy [14, 15].

However, unlike the plasma corona, this region is optically thick, which implies that there is a strong reabsorption of emitted photons and, hence, opacity effects must be taken into account.

In principle, one can also use XUV interferometry (for instance, with XUV laser sources), but in reality, this is quite challenging [16].

The shocked region is particularly difficult to be probed. Due to its low temperature, there is no strong emission of radiation (and this is concentrated at long wavelength), and because of its large density, this is very opaque. One can use X-ray radiography using hard X-ray emitted from a secondary laser-produced plasma [17] or (with care) proton radiography (PR) [18]. It is also possible to use optical diagnostics on the target 'rear side', if a thin target is used, and the shock finally breaks out on the rear side [19–21].

To complete the panorama, one should cite all diagnostics that are typical for laser-driven inertial fusion experiments: neutron measurements [22], neutron spectroscopy [23], and neutron imaging [24].

Of course it is not possible to deal with all such different diagnostics in a single paper. Therefore, we will just concentrate on a few recent examples of diagnostics.

Spherically bent crystal for X-ray imaging

X-ray imaging is very important in order to study laser-produced plasmas [25]. One tool is at the same time rather simple and very powerful and has found a very large application in recent experiment. This is the use of spherically bent crystals [26, 27].

In particular, spherically bent crystals have been used to provide information on hot electron transport in dense plasmas. Such a study is fundamental for high energy density physics (HEDP) research [28, 29], from experimental astrophysics to fast ignition (FI) studies. In the FI scheme, for example, the compressed deuterium-tritium (DT) fuel is heated by an ultra-intense laser-generated fast electron beam, which carries the laser energy from the critical surface and deposits it in the DT fuel [30]. More in general, for HEDP studies, the fast electron beam can be used for fast (picosecond scale) plasma heating [31] as well as to generate pulsed X-ray sources to perform temporally resolved radiography of ultra-fast plasma phenomena such as shock propagation through target samples [17].

In this context, a characterization of the fast electron beam is highly desirable. The spherically bent crystal for two-dimensional imaging is a powerful diagnostic, allowing obtaining both qualitative and quantitative information on the fast electron transport.

A fast electron beam propagating through a dense medium releases its energy in many ways. Therefore, the stopping power is composed by several terms [32]:

$$\frac{dE}{dx} = \frac{4\pi e^4}{E}\left[n_b L_b + n_f\left(L_f + L_W\right)\right] \tag{2}$$

where L_b, L_f, and L_W are, respectively, the stopping numbers for interaction with bound electrons, free electrons, and generation of plasma waves. The Bremsstrahlung term has been omitted here because it is important for very high-energy electrons and high Z materials. The term of direct interest for the spherically bent crystal is L_b. The interaction of fast electron beam with a bound electron could result in the collisional ionization of the atom, followed by recombination and emission of a photon. In case the vacancy is generated in the inner electronic shells of an atom, the emitted radiation is in the X-ray domain. In particular, if a vacancy is created in the innermost shell, the so-called K shell, the emitted photon will be a Kα photon. Kα radiation is particularly interesting because electrons in K shell of an atom are the most strongly bounded

and consequently have the highest ionization potential E_K; therefore, recording Kα radiation provides information about the transport of electrons with energy $E > E_K$.

In general, the cross section of K-shell ionization is provided by the following equation:

$$\sigma_K(E)\,[\mathrm{cm}^2] = 7.92\times10^{-14} R(E)\frac{1}{EE_K}\ln\frac{E}{E_K} \tag{3}$$

where $R(E)$ is a relativistic correction factor to the original equation and influences the cross section of ultra-relativistic incident electron energies ($E >$ 1 MeV).

Being the Kα emission completely isotropic, imaging the X-ray source corresponds to image the fast electron path through the material.

A spherically bent crystal can be used to obtain 2D spatially resolved, monochromatic images of a Kα source. The diagnostic is based on the well-known Bragg reflection law:

$$2d \sin\theta_B = n\lambda \tag{4}$$

where θ_B is the Bragg angle and d is the crystal interatomic spacing.

To ensure high imaging quality, the Bragg angle must be close to 90°, resulting in a reduced availability of crystals to efficiently image Kα radiation emitted by different elements. Two of the most widely used crystals are Quartz 211 ($2d$ = 2.749 Å) and Quartz 203 ($2d$ = 3.082 Å), respectively, reflecting the Cu-Kα line (8.047 keV) and the Ti-Kα line (4.510 keV) having Bragg angles, respectively, of 88.7° and 89.1°. The focusing property of the crystal, determined by its spherical bending, together with the quasi-normal X-ray reflection, makes it an imaging device, described as a spherical mirror:

$$\frac{1}{p}+\frac{1}{q}=\frac{2}{R} \tag{5}$$

where p and q are, respectively, the image and the object distance from the mirror on the optical axis and R is the curvature radius of the crystal. In general, this equation has the straightforward solution

$$p=\frac{qR}{2p-R} \tag{6}$$

The Kα imager is an intrinsically astigmatic optical system, being the source, and consequently the image, off-axis. The X-ray detector (usually an X-ray charge-coupled device (CCD) camera or an image plate) has, therefore, to be positioned between the meridional and the sagittal focal position, close to the so-called circle of least confusion, in order to maximize the spatial resolution of the image (see Fig. 1). The sagittal and meridional focal positions are determined by the crystal curvature radius as well as the Bragg angle as follows:

$$p_s=\frac{qR}{2q\sin\theta_B - R},\quad p_m=\frac{qR\sin\vartheta_B}{2q - R\sin\theta_B} \tag{7}$$

The astigmatism-limited spatial resolution for ideal alignment is given by

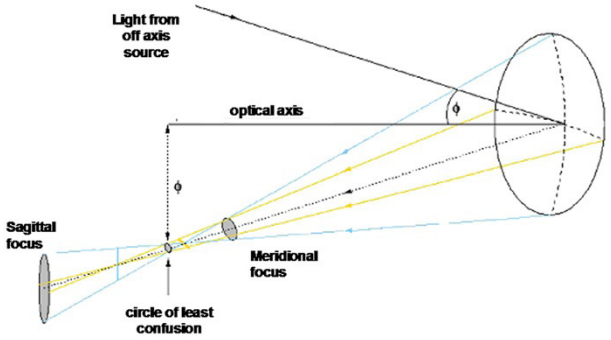

Fig. 1. Spherically bent mirror with off-axis source. The astigmatism results in two focal points, the meridional and the sagittal foci. The maximum resolution is obtained at the intermediate point between the foci, corresponding to the circle of least confusion.

$$\sigma=\frac{M+1}{M}(1-\sin\theta_B)D \tag{8}$$

where M is the magnification of the system ($M = p/q$) and D is the aperture limiting the reflecting area of the crystal.

For a typical alignment setup, the optical resolution can be as high as 5 μm, whence the measured value in the X-rays is often larger, typically between 10 and 20 μm.

This difference is explained accounting for the bending quality of the crystal. In many cases, in fact, mostly when the curvature radius is small, the bending process introduces several cracks in the crystal, resulting in a mosaic structure and affecting the overall resolution of the optical system.

Applications

Early experiments on fast electron transport in solid density plasmas were focused on understanding the fast electron penetration depth in a target material as well as the fast electron beam divergence.

The fast electron penetration depth in target material was measured by using multilayer targets. The first layer being made by the material in which we want to investigate the fast electron penetration depth, followed by a thin tracer layer (Cu or Ti), and finally, by a third layer to prevent Kα radiation produced by the refluxing electrons. Varying the thickness of the first layer, it is possible to estimate the fast electron penetration depth by integrating the Kα signal obtained for each overcoating thickness and fitting it with an exponential function such as

$$f(x) = Ae^{-x/\lambda} \tag{9}$$

where λ is the penetration depth (see Fig. 2).

As for fast electron divergence and spatial information, such measurements are fundamental for a number of applications, including fast electron (FI). To determine this quantity, it is necessary to measure the Kα spot size for different overcoating thicknesses, in a similar manner as the measurement presented in the next section. Typical values for the

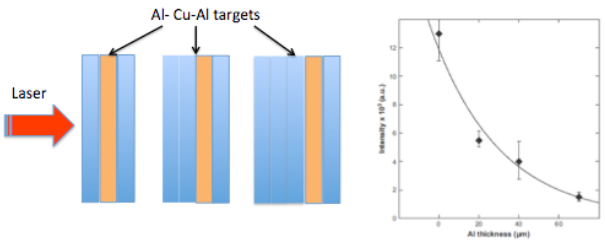

Fig. 2. (left) Multilayer targets with variable transport layer thickness and Cu tracer layer are used to determine the fast electron penetration depth (right). This target design is also used to measure the fast electron divergence in the target material (data and figures adapted from [27]).

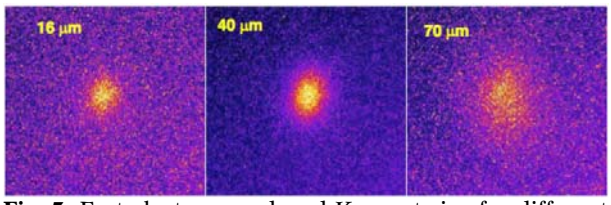

Fig. 3. Fast electron produced Kα spot size for different overcoating corresponding to 16, 40, and 70 μm (data and figures adapted from [27]).

fast electron divergence in solid density plasmas are 40–50° (see Fig. 3).

VISAR

The VISAR (velocity interferometer system for any reflector) is an interferometric active diagnostic that allows measuring the Doppler effect induced by the movement of a reflective surface using a probe beam that illuminates this moving surface. It has been introduced by researchers from Los Alamos [33], and later, it has been mainly used for experiments relative to laser-driven shock and studies of materials at extreme pressures [34, 35]. In this context, it has found recent applications for shock-timing in the context of implosion experiments on the National Ignition Facility [36].

VISAR is based on the Mach-Zehnder interferometer in which we introduce an etalon (typically a piece of glass with antireflection coating) followed by a streak camera in order to obtain time-resolved measurement.

In a classical Mach-Zehnder interferometer (see Fig. 4), the probe beam is first divided in two beams at the entrance of the system by a beamsplitter (BS1). Both beams are reflected on a mirror (M1 and M2) and are recombined at the outer surface of the second beamsplitter (BS2). Eventually, we image the interferometric pattern from the BS2 into a screen or, in our case, on a CCD for alignment and on the slit of the streak camera for measurement.

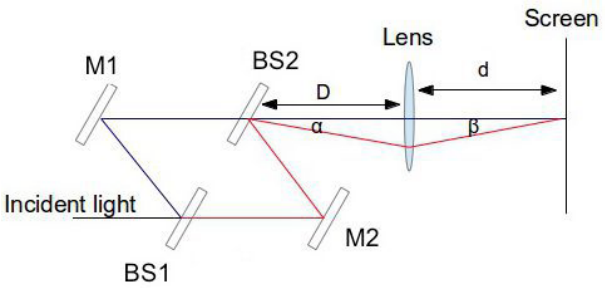

Fig. 4. Scheme of the Mach-Zehnder interferometer with small angle.

Here, M1 and M2 are parallel and both arms have the same length. BS2 has a small angle compared to BS1, which creates fringes of equal thickness (similar to that of a Michelson interferometer in air corner configuration). We obtain the expression of the interfringe with the small angle hypothesis:

$$i = \frac{\lambda d}{D\alpha} \tag{10}$$

So, if we only consider the Mach-Zehnder interferometer, it would be possible to measure the Doppler effect by measuring the variation of the interfringe. However, this variation is so small that would not be possible to see any result with our measurement system (the typical result would be a variation of a few nanometers of the interfringe which is not compatible with streak camera precision).

This is the reason why we improve this interferometer by using an etalon of reflective index n, thickness e, and with antireflection coatings on both sides. By placing this etalon in front of M1, we induce a refraction of the beam and an increase in the optical path. To compensate this loss of spatial coherence, we mount the mirror M1 on a motor stage to compensate it by moving it of the distance:

$$d = e\left(1 - \frac{1}{n}\right) \tag{11}$$

This correction permits overlapping the images of the two arms on the same point even with a diffusive reflection and assures the spatial coherence of the image on BS2.

With the etalon placed in the interferometer, any change in the velocity of the reflecting surface imaged on the output beamsplitter will results in a phase shift in the interference pattern. The fringe shift is then related to the velocity of the surface by:

$$F(t) = \frac{\Delta\phi(t)}{2\pi} = \frac{2\tau_0(1+\delta)}{\lambda_0} v(t) \tag{12}$$

where $\phi(t)$ is the phase of the fringe and τ_0 the initial delay without taking into account the variation of refractive index related with the Doppler effect:

$$\tau_0 = \frac{2e}{c}\left(n_0 - \frac{1}{n_0}\right) \tag{13}$$

and δ is the corrective term associated with the spectral dispersion of the etalon:

$$\delta = -\left(\frac{n_0}{n_0^2 - 1}\right)\lambda_0 \left(\frac{dn}{d\lambda}\right)_{\lambda=\lambda_0} \tag{14}$$

So, if we want to measure a high speed, we need to use a thin etalon.

Another problem is that when the reflecting surface is put in motion by the breakout of a shock, the measured velocity passes from 0 to a high velocity within a short time that cannot be seen in the streak image. In that case, we only see a discontinuity in the

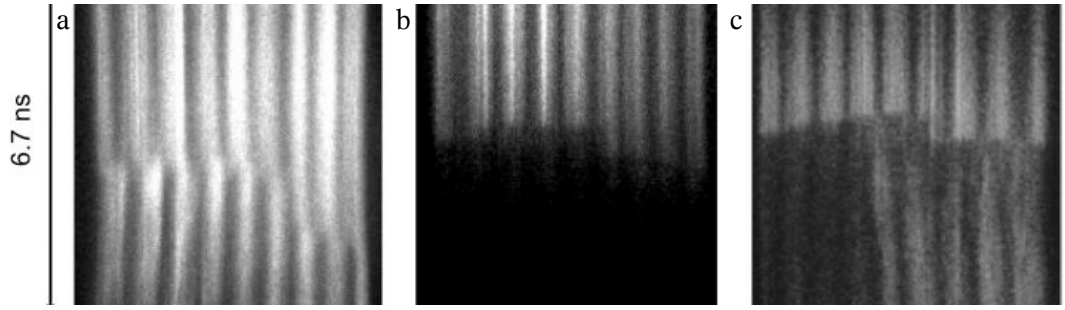

Fig. 5. Examples of shock velocity measurement using a VISAR in three different regimes. The compressed material is (a) transparent (here water), (b) completely opaque, (c) metalized (figures adapted from [37]).

fringe shift, and it is impossible to know the exact number of fringes that we jumped. Indeed, we can only measure the decimal part of the fringes shift, and in order to remove the incertitude, we need to use two different VISARs with two different sensitivities (not proportional).

One of the key issues of this diagnostic is the alignment of the interferometric part. First, you need to build a line with the probe beam that illuminates the backside of the target on a big enough zone (two or three times the size of the focal spot) and then image it on the outer plane of the BS2 and then on the streak slit. Then, you need to align the interferometric part (the two mirrors and the two beamsplitters). This alignment is quite time consuming and can be complicated especially when we want to be very accurate.

The VISAR can measure not only the velocity of a surface put into motion by a shock breakout as said before but also the shock breakout time (see the discontinuity in Fig. 5a–c). In the case of a transparent material, it measures the velocity of the shock front when it metalizes the material it is propagating in (e.g., quartz, diamond, or water like in Fig. 5c) and the fluid velocity (Fig. 5a) if it does not make the material opaque (Fig. 5b) because it only measures the difference in refractive index on the material because of its compression. Another magnitude that the VISAR can measure is the reflectivity of the surface by considering the intensity of the fringes in comparison with a measured reference.

They are many applications of this diagnostics. We can quote, for example, shock ignition experiments or experiment of equation of state measurement. There are several ways of using it. First, we can measure the velocity of a free surface of a material where a shock is propagating. Then, we can measure the velocity of a shock inside a transparent material (if this material is the material we are studying). Eventually, we can measure the velocity inside a reference material (e.g., alpha-quartz) in order to infer the pressure in the material before it by impedance mismatch.

Before using this diagnostic, one has to check whether it can be used. Indeed, there are conditions that make it useless or inefficient to measure anything. Among them, we highlight the following conditions:

- Angular acceptance: the shock has to be flat enough in order to reflect the light inside the cone of the last lens.
- Preheating: when measuring the velocity through a transparent window, hot electrons have to be stopped and should not reach the windows because when they reach it, then can ionize the material which become then opaque.
- Blanking: when the shock is very strong, it blinds the streak camera and we do not see anything (black image on the streak).

When using this diagnostic, the process to obtain useful result is simpler. However, before trying to get any velocity, some basic treatments has to be performed on the images to erase some systematic error sources. First, two images have to be recorded: the image while the shock is propagating and, before the shot, an image where the probe laser is just reflected at the rear surface of the target in order to be sure that the fringes are straight when there is no shock. After, on any image, we can see that even after the propagation of the shock, we still see some fringes. These fringes are called ghost fringes, they are due to the surface quality of the optics and some additional reflection they can generate. Ghost fringes have to be erased on all the images to obtain the real signal.

So, depending on the application, the VISAR can be a direct or an indirect measurement of the velocity with a sensitivity that can be tuned by changing the etalon.

Proton radiography

Laser-based protons have developed during the past 10 years and have been applied to many experiments to study electron beam propagation in warm dense matter (WDM), to validate the FI approach to inertial-confinement fusion, to study in general HEDP. Laser-based proton beams can be generated by irradiating a thin metal layer (usually gold or titanium) with an ultra-short (from picoseconds to femtosecond), ultra-high intensity ($I \sim 10^{19-21}$ W/cm^2) laser beam. They are characterized by a small source, high degree of collimation, and a short duration [38–42].

A typical PR setup is shown in Fig. 6: protons, generated via laser-target interaction, probe the imploding target and are stopped inside the radiochromic films (RCF) stack as a function of their energy. If the proton beam is multienergetic, then protons with different energies arrive at different times (time of flight) to probe the target and are stopped at different positions inside the detector. Moreover, because of the Bragg peak properties, protons deposit most of the energy at the end of their travel inside the matter. This fact permit us to arrange the positions of

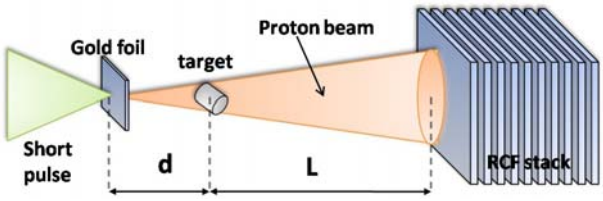

Fig. 6. Scheme of proton radiography.

the films inside the stack in order to associate each film with a given detected proton energy. Finally, if the target is dropped leaving free space between the source and the detector and because the proton spectrum decreases rapidly with increasing energy, the contribution of higher-energy protons in a given RCF can be neglected. Consequently, each RCF can be associated with a single instant of the implosion history.

This scheme has been used many times to infer the proton beam spectrum starting from the images obtained in the RCFs and using a deconvolution technique. In inertial-confinement fusion (ICF) experiments, the proton spectrum changes drastically after that protons penetrate the core of the imploding target leading to a mixing of the images formed by protons with different energies. Owing to the very large mass densities reached during target implosion, protons travelling through the target undergo a very large number of collisions, which deviate them from straight trajectories and reduce the PR resolution below our expectations.

The following analytical evaluation of the multiple scattering (MS) effects on PR resolution allows to evaluate the correct object size and the necessary parameters conditions. The effect of MS on the detected size of the cylinder is described by the blurring factor ξ

$$\xi = L\langle\vartheta\rangle$$

$$\langle\vartheta\rangle = \frac{E_s[\mathrm{MeV}]}{2}\sqrt{\frac{1}{L_R\left[\mathrm{g/cm^2}\right]}}\frac{\sqrt{A\left[\mathrm{g/cm^2}\right]}}{E[\mathrm{MeV}]} \tag{15}$$

$$A = \int_{-\infty}^{\infty}\rho(x)dx$$

where A is the areal density, L is the cylinder-detector distance, and $<\theta>$ is the mean angular scattering of a proton with energy E_s traversing a material with density ρ as was obtained by Rossi and Greisen [43]. Finally, $E_s = 15$ MeV and L_R is the radiation length.

A criterion to estimate PR resolution starting from the experimental parameters can be defined by considering the experimental setup shown in Fig. 7 in which a point-like proton source irradiates a finite-size object, projecting its image onto a detector. In principle, if the MS is negligible, protons do not deviate from their trajectories and the projected image size will appear enlarged by a factor $M = (L + d)/d$, which corresponds to geometrical magnification.

In particular, defining a generic finite distance between two points δx, the projected size on the detector becomes $\Delta_x = M\delta_x$. Nevertheless, the effect of the MS is never negligible and the protons passing through the object are deflected by a mean

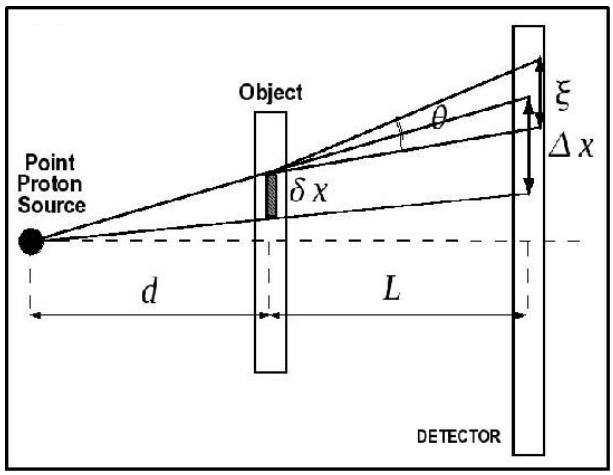

Fig. 7. Scheme for the calculation of PR resolution.

angle $<\theta>$, giving a mean displacement $\xi = L <\theta>$, which can be estimated using Eq. (1). Therefore, the projected image on the detector will appear enlarged by a factor μ, with respect to that which would appear if there were no scattering Δ_x, that is, by a factor μM with respect to the initial size δ_x, where μ is defined as follows:

$$\bar{\xi} = \sqrt{1 + \left(\frac{\xi}{\delta x}\right)^2}, \quad \bar{\xi} = \xi / M \tag{16}$$

Starting from the above considerations, we can infer that the blurring coefficient must remain less than or of the same order on the resolution that we would like to obtain, δx, in order to avoid a cross-over between different single-proton trajectories and to prevent a consequent loss of the initial spatial target information carried on by protons. The above-mentioned condition can be written in terms of the blurring coefficient (i.e., ξ is the resolution of our system in analogy with the Rayleigh criterion in optics)

$$0 \le \bar{\xi} \le \delta x \tag{17}$$

or in terms of the unit-less parameter μ,

$$0 \le \mu \le \sqrt{2} \tag{18}$$

If such condition is satisfied, the PR can be used in the conventional way, and the grey scale level obtained from the RCF analysis will be proportional to the density gradient of the probed target. A simple estimate of the μ parameter can be done by considering the protons passing through the dense core of imploding plasma. Let us assume that the size of the core to be ~60 μm, we look for a resolution $d_x \sim$ 20 μm; the blurring coefficient $<\xi>$ can be estimated by assuming the maximum reached energy for protons (10 MeV), which are passing through an area density $A \sim 0.05$ g/cm^2 for a magnification factor $M = 4.5$. The result is $\mu \sim 7$, which is larger than the minimum permitted value, confirming that at the relatively small energy (~40–50 MeV), laser-driven proton beams obtained efficient PR resolution cannot be achieved because proton beams are not able to probe the dense core of the imploding target.

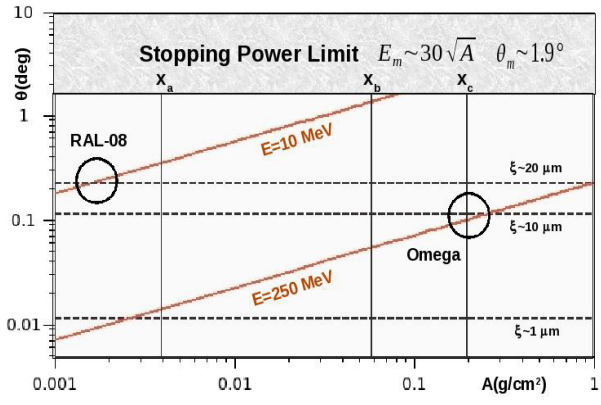

Fig. 8. Mean scattering angle θ vs. areal density for different proton energies. x_a: $A \sim 0.004$ g/cm^2 proton trajectory calculated through plasma corona, x_b: $A \sim 0.05$ g/cm^2 trajectory through core for the present experiment; and x_c: $A \sim 0.2$ g/cm^2 trajectory (theory) for a typical Omega target. If we assume $d = L = 1$ cm ($M = 2$), we get the corresponding spatial resolution limits: ~20 μm, ~10 μm or ~1 μm. The grey region corresponds to the SP limit $\theta_{max} \sim 1.9°$.

On the other hand, considering protons passing through the plasma's corona, the areal density becomes $A \sim 0.002$ g/cm^2, and at the same conditions, we obtain μm ~ 2, which corresponds to a resolution no larger than 20 μm. The graph in Fig. 8 summarizes PR resolution as a function of the probed plasma area density for different proton energies.

The above-mentioned analysis shows that PR resolution depends also on the spatial properties of the plasma, this fact has been analytically investigated in Ref. [42] where was shown the dependence of PR resolution on the plasma density profile. Here, as an example, we show some results on PR resolution performance by using Monte Carlo (MC) simulations. The plasma effects are considered by modifying the density profile included in the MC code. In these cases, the chosen profile is arbitrary; so for simplicity, the plasma effects have not been taken into account, changing only the density profiles. The stopping power for protons in the target is described by using Bethe's theory [44], while MS effects are described by using Rossi's theory [43]. A detailed description of the time-dependent MC simulation process can be found in Refs. [40, 45].

MC simulations are performed by assuming $E_p = 20$ MeV proton beam probing a spherical target with variable $\gamma = 2, 4, 6$ (where γ is the degree of a super-Gaussian profiles) density profiles ($\rho_p = 6$ g/cm^3, w = FWHM/2, $w = 100$ μm) that correspond to a peak areal density A ($y = 0$) ~ 0.12 g/cm^2. Simulation results shown in Fig. 9 confirm the analytical prediction in Ref. [41].

Conclusions

This paper was addressed to give a few examples of the large variety of diagnostics that are needed to study the laser-produced plasmas. Of course a complete presentation would imply a full book.

Our choice has been motivated not only by the fact that we have presented some diagnostics adapted to the different plasma regions and diagnostic goals but also by the fact that all these represent novel development that have been largely used in recent experimental research in the past 10 years.

Acknowledgments. We acknowledge the support of COST Action MP1208 "Developing the physics and the scientific community for inertial fusion".

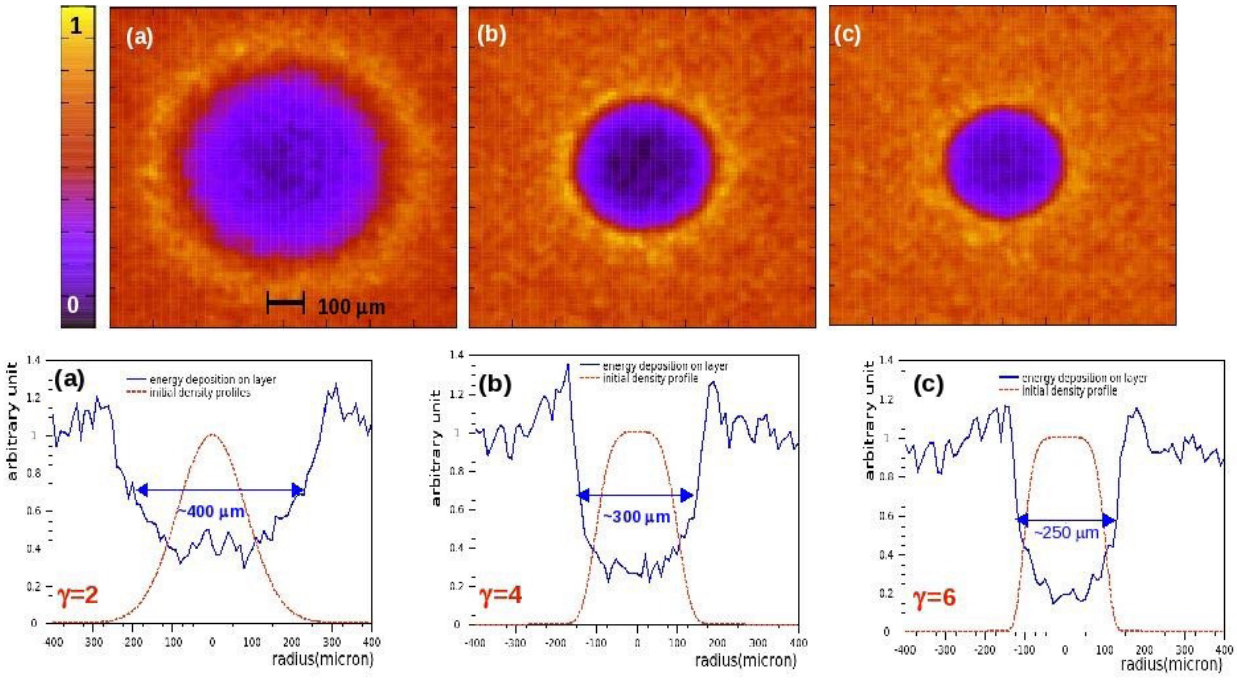

Fig. 9. Monte Carlo simulations of a spherical target with variable super Gaussian density profile probed by a 10-MeV proton beam. Two-dimensional map view of the probed target (top). One-dimensional profile obtained from line out of 2D map compared with initial density profile (bottom).

References

1. Aliverdiev, A., Batani, D., Dezulian, R., Vinci, T., Benuzzi-Mounaix, A., Koenig, M., & Malka, V. (2008). Coronal hydrodynamics of laser-produced plasmas by interferometry. *Phys. Rev. E*, *78*, 046404.
2. Lancaster, K. L., Pasley, J., Green, J. S., Batani, D., Baton, S., Evans, R. G., Gizzi, L., Heathcote, R., Hernandez Gomez, C., Koenig, M., Koester, P., Morace, A., Musgrave, I., Norreys, P. A., Perez, F., Waugh, J., & Woolsey, N. (2009). Temperature profiles derived from transverse optical shadowgraphy in ultra-intense laser plasma interactions at 6 x 10^{20} W/cm^2. *Phys. Plasmas*, *16*, 056707.
3. Manclossi, M., Batani, D., Piazza, D., Baton, S., Amiranoff, F., Koenig, M., Popescu, H., Audebert, P., Santos, J. J., Martinolli, E., Rabec Le Gloahec, M., Antonicci, A., Rousseaux, C., Borghesi, M., Cecchetti, C., Malka, V., & Hall, T. (2005). Optical shadowgraphy and proton imaging as diagnostics tools for fast electron propagation in Ultra-High-Intensity Laser-Matter interaction. *Radiat. Eff. Defects Solids*, *160*, 575–585.
4. Stamper, J. A., & Ripin, B. H. (1975). Faraday-rotation measurements of megagauss magnetic fields in laser-produced plasmas. *Phys. Rev. Lett. 34*(3), 138. http://dx.doi.org/10.1103/PhysRevLett.34.138.
5. Rosmej, F., Faenov, A., Pikuz, T., Flora, F., Di Lazzaro, P., Bollanti, S., Lisi, N., Letardi, T., Reale, A., Palladino, L. Batani, D., Bossi, S., Bernardinello, A., Scafati, A., Reale, L., Zigler, A., Fraenkel, M., & Cowan, E. (1997). Inner-shell satellite transitions in dense short pulse plasmas. *J. Quant. Spectrosc. Radiat. Transf*., *58*, 859–878.
6. Martinolli, E., Koenig, M., Boudenne, J. M., Perelli-Cippo, E., Batani, D., & Hall, T. A. (2004). Conical crystal spectrograph for high brightness X-ray K alpha spectroscopy in subpicosecond laser-solid interaction. *Rev. Sci. Instrum*., *75*, 2024.
7. Nishimura, H., Inubushi, Y., Okano, Y., Fujioka, S., Kai, T., Kawamura, T., Batani, D., Morace, A., Redaelli, R., Fourment, C., Santos, J., Malka, G., Boscheron, A., Casner, A., Koenig, M., Nakamura, T., Johzaki, T., Nagatomo, H., & Mima, K. (2008). X-ray polarization spectroscopy to study energy transport in ultra-high intensity laser produced plasmas. *J. Phys*., *112*, 022080.
8. Koenig, M., Boudenne, J. M., Legriel, P., Grandpierre, T., Batani, D., Bossi, S., Nicolella, S., & Benattar, R. (1997). A computer driven crystal spectrometer with CCD detectors for X-ray spectroscopy of laser-plasmas. *Rev. Sci. Instrum*., *68*, 2387.
9. Stepanov, A., Starostin, A., Roerich, V., Makhrov, V., Faenov, A., Magunov, A., Pikuz, T., Skobelelev, I., Flora, F., Bollanti, S., Di Lazzaro, P., Lisi, N., Letardi, T., Palladino, L., Reale, A., Batani, D., Bossi, S., Bernardinello, A., Scafati, A., Reale, L., Osterheld, A., & Goldstein, W. (1997). Modelling of the He-like magnesium spectral line radiation from the plasma created by XeCl and Nd-glass lasers. *J. Quant. Spectrosc. Radiat. Transf.*, *58*(4/6), 937–952.
10. Batani, D., Bianconi, F., Giulietti, A., Giulietti, D., & Nocera, L. (1989). Second harmonic polarisation and conversion efficiency in laser produced sparks. *Opt. Commun*., *70*(1), 38–43.
11. Giulietti, A., Giulietti, D., Batani, D., Biancalana, V., Gizzi, L., Nocera, L., & Schifano, E. (1989). Spectroscopic evidence for sum frequency of forward and backscattered light in laser plasmas. *Phys. Rev. Lett*., *63*, 524.
12. Giulietti, D., Biancalana, V., Batani, D., Giulietti, A., Gizzi, L., Nocera, L., & Schifano, E. (1991). Three half harmonic generation in laser plasma interaction: evidence for plasmon propagation. *Il Nuovo Cimento D*, *13*(7), 845–858.
13. Antonelli, L., Batani, D., Patria, A., Ciricosta, O., Cecchetti, C., Koester, P., Labate, L., Giulietti, A., Gizzi, L. A., Moretti, A., Richetta, M., Giuffrida, L., Torrisi, L., Kozlova, M., Nejdl, J., Sawicka, M., Margarone, D., Rus, B., Schurtz, G., Ribeyre, X., Lafon, M., Spindloe, C., & O'Dell, T. (2011). Laser-plasma coupling in the shock-ignition intensity regime. *Acta Tecnica*, *56*, T57.
14. Pisani, F., Koenig, M., Batani, D., Hall, T., Desenne, D., Bruneau, J., & Reverdin, C. (1999). Toroidal crystal spectrometer for time-resolved X-ray absorption diagnostic in dense plasmas. *Rev. Sci. Instrum*., *70*, 3314.
15. Hall, T., Al-Kuzee, J., Benuzzi, A., Koenig, M., Krishnan, J., Grandjouan, N., Batani, D., Bossi, S., & Nicolella, S. (1998). Experimental observation of the shift and width of the aluminium K absorption edge in laser shock compressed plasmas. *Europhys. Lett*., *41*(5), 495–500.
16. Batani, D., Antonelli, L., Atzeni, S., Badziak, J., Baffigi, F., Chodukowski, T., Consoli, F., Cristoforetti, G., de Angelis, R., Dudzak, R., Folpini, G., Giuffrida, L., Gizzi, L. A., Kalinowska, Z., Koester, P., Krousky, E., Krus, M., Labate, L., Levato, T., Maheut, Y., Malka, G., Margarone, D., Marocchino, A., Nejdl, J., Nicolai, Ph., O'Dell, T., Pisarczyk, T., Renner, O., Rhee, Y. J., Ribeyre, X., Richetta, M., Rosinski, M., Sawicka, M., Schiavi, A., Skala, J., Smid, M., Spindloe, Ch., Ullschmied, J., Velyhan, A., & Vinci, T. (2014). Generation of high pressure shocks relevant to the shock-ignition intensity regime. *Phys. Plasmas*, *21*, 032710.
17. Ravasio, A., Koenig, M., Le Pape, S., Benuzzi-Mounaix, A., Park, H. S., Cecchetti, C., Patel, P., Schiavi, A., Ozaki, N., Mackinnon, A., Loupias, B., Batani, D., Boehly, T., Borghesi, M., Dezulian, R., Henry, E., Notley, M., Bandyopadhyay, S., Clarke, R., & Vinci, T. (2008). Hard x-ray radiography for density measurement in shock compressed matter. *Phys. Plasmas*, *15*, 060701.
18. Ravasio, A., Le Pape, S., Benuzzi-Mounaix, A., Romagnani, L., Cecchetti, C., Batani, D., Boehly, T., Borghesi, M., Dezulian, R., Gremillet, L., Henry, E., Hicks, D., Loupias, B., McKinnon, A., Ozaki, N., Park, H. S., Patel, P., Schiavi, A., Vinci, T., Clarke, R., Notley, M., Bandyopadhyay, S., & Koenig, M. (2010). Proton radiography of a shock compressed target. *Phys. Rev. E*, *82*, 016407.
19. Koenig, M., Faral, B., Boudenne, J. M., Batani, D., Bossi, S., & Benuzzi, A. (1994). Use of optical smoothing techniques for shock wave generation in laser produced plasmas. *Phys. Rev. E-Rapid Commun*., *50*, R3314–R3317.
20. Benuzzi, A., Nazarov, V., Koenig, M., Krishnan, J., Faral, B., Temporal, M., Batani, D., Muller, L., Torsiello, F., Hall, T., & Grandjouan, N. (1998). Dynamics of laser produced shocks in foam-solid targets. *Phys. Plasmas Lett.*, *5*, 2827–2829.
21. Batani, D., Benuzzi, A., Koenig, M., Krasyuk, I., Pashinin, P., Semenov, A., Lomonosov, I., & Fortov, V. (1999). Problems of measurement of dense plasma heating in laser shock wave compression. *Plasma Phys. Control. Fusion*, *41*, 93–103.
22. Skupsky, S., & Kacenjar, S. (1981). Measuring fuel ρR for inertial fusion experiments using neutron elastic-scattering reactions. *J. Appl. Phys*., *52*, 2608.

23. Frenje, J. A., Casey, D. T., Li, C. K., Rygg, J. R., Séguin, F. H., Petrasso, R. D., Glebov, V. Yu., Meyerhofer, D. D., Sangster, T. C., Hatchett, S., Haan, S., Cerjan, C., Landen, O., Moran, M., Song, P., Wilson, D. C., & Leeper, R. J. (2008). First measurements of the absolute neutron spectrum using the magnetic recoil spectrometer at OMEGA. *Rev. Sci. Instrum.*, *79*, 10E502.
24. Caillaud, T., Landoas, O., Briat, M., Kime, S., Rossé, B., Thfoin, I., Bourgade, J. L., Disdier, L., Glebov, V. Yu., Marshall, F. J., & Sangster, T. C. (2012). Development of the large neutron imaging system for inertial confinement fusion experiments. *Rev. Sci. Instrum.*, *83*, 033502.
25. Giulietti, D., & Gizzi, L. A. (1998). X-ray emission from laser-produced plasmas. *La Rivista del Nuovo Cimento*, *21*, 1.
26. Antonelli, L., Forestier-Colleoni, P., Folpini, G., Bouillaud, R., Faenov, A., Fedeli, L., Fourment, C., Giuffrida, L., Hulin, S., Pikuz, S., Santos, J. J., Volpe, L., & Batani, D. (2015). Measurement of reflectivity of spherically bent crystals using Kα signal from hot electrons produced by laser-matter interaction. *Rev. Sci. Instrum.*, *86*, 073507.
27. Morace, A., & Batani, D. (2010). Spherically bent crystal for X-ray imaging of laser produced plasmas. *Nucl. Instrum. Methods Phys. Res. Sect. A-Accel. Spectrom. Dect. Assoc. Equip.*, *623*(22), 797–800.
28. Stephens, R. B., Aglitskiy, Y., Amiranoff, F., Andersen, C., Batani, D., Baton, S. D., Cowan, T., Freeman, R. R., Hall, T., Hatchett, S. P., Hill, J. M., Key, M. H., King, J. A., Koch, J. A., Koenig, M., MacKinnon, A. J., Lancaster, K. L., Martinolli, E., Norreys, P., Perelli-Cippo, E., Rabec Le Gloahec, M., Rousseaux, C., Santos, J. J., Scianitti, F., & Snavely, R. A. (2004). Kα fluorescence measurement of relativistic electron transport in the context of fast ignition. *Phys. Rev. E*, *69*, 066414.
29. Freeman, R. R., Batani, D., Baton, S., Key, M., & Stephens, R. (2006). The generation and transport of large currents in dense materials: The physics of electron transport relative to fast ignition. *Fusion Sci. Technol.*, *49*(3), 297–315.
30. Batani, D. (2011). Studies on fast electron transport in the context of fast ignition. *Nukleonika*, *56*(2), 99–106.
31. Baton, S. D., Koenig, M., Guillou, P., Loupias, B., Benuzzi-Mounaix, A., Fuchs, J., Rousseaux, Ch., Gremillet, L., Batani, D., Morace, A., Nakatsutsumi, M., Kodama, R., & Aglitskiy, Y. (2007). Relativistic electron transport and confinement within charge-insulated, mass-limited targets. *High Energy Density Phys.*, *3*(3/4), 358–364.
32. Batani, D. (2002). Transport in dense matter of relativistic electrons produced in utra-high-intensity laser interactions. *Laser Part. Beams*, *20*(02), 321–336.
33. Barker, L. M. (2000). The development of the VISAR, and its use in shock compression science. *AIP Conf. Proc.*, *505*, 11.
34. Benuzzi-Mounaix, A., Koenig, M., Huser, G., Faral, B., Grandjouan, N., Batani, D., Henry, E., Tomasini, M., Marchet, B., Hall, T. A., Boustie, M., De Rességuier, Th., Hallouin, M., & Guyot, F. (2002). Absolute equation of state measurements of iron using laser driven shocks. *Phys. Plasmas*, *9*, 2466.
35. Batani, D., Morelli, A., Tomasini, M., Benuzzi-Mounaix, A., Faral, B., Koenig, M., Baclet, P., Cathala, B., Marchet, B., Masclet, I., Rebec, M., Reverdin, Ch., Cauble, R., Celliers, P., Collins, G., Da Silva, L., Hall, T., Moret, M., & Sacchi, B. (2002). Equation of state data for Iron at pressure beyond 10 Mbar. *Phys. Rev. Lett.*, *88*, 235502.
36. Munro, D. H., Celliers, P. M., Collins, G. W., Gold, D. M., Da Silva, L. B., Haan, S. W., Cauble, R. C., Hammel, B. A., & Hsing, W. W. (2001). Shock timing technique for the National Ignition Facility. *Phys. Plasmas*, *8*, 2245.
37. Batani, D., Jakubowska, K., Benuzzi-Mounaix, A., Cavazzoni, C., Danson, C., Hall, T., Kimpel, M., Neely, D., Pasley, J., Rabec Le Gloahec, M., & Telaro, B. (2015). Refraction index of shock compressed water in the megabar pressure range. *Europhys. Lett.*, *112*(3), 36001.
38. Mackinnon, A. J., Patel, P. K., Borghesi, M., Clarke, R. C., Freeman, R. R., Habara, H., Hatchett, S. P., Hey, D., Hicks, D. G., Kar, S., Key, M. H., King, J. A., Lancaster, K., Neely, D., Nikkro, A., Norreys, P. A., Notley, M. M., Phillips, T. W., Romagnani, L., Snavely, R. A., Stephens, R. B., & Town, R. P. J. (2006). Proton radiography of a laser-driven implosion. *Phys. Rev. Lett.*, *97*(4), 045001.
39. Borghesi, M., Mackinnon, A. J., Campbell, D. H., Hicks, D. G., Kar, S., Patel, P. K., Price, D., Romagnani, L., Schiavi, A., & Willi, O. (2004). Multi-MeV proton source investigations in ultraintense laser-foil interactions. *Phys. Rev. Lett. 92*(5), 055003.
40. Batani, D., Baton, S. D., Manclossi, M., Piazza, D., Koenig, M., Benuzzi-Mounaix, A., Popescu, H., Rousseaux, C., Borghesi, M., Cecchetti, C., & Schiavi, A. (2009). LASER-driven fast electron dynamics in gaseous media under the influence of large electric fields. *Phys. Plasmas*, *16*, 033104.
41. Volpe, L., Batani, D., Vauzour, B., Nicolai, Ph., Santos, J. J., Regan, C., Morace, A., Dorchies, F., Fourment, C., Hulin, S., Perez, F., Baton, S., Lancaster, K., Galimberti, M., Heathcote, R., Tolley, M., Spindloe, Ch., Koester, P., Labate, L., Gizzi, L. A., Benedetti, C., Sgattoni, A., Richetta, M., Pasley, J., Beg, F., Chawla, S., Higginson, D. P., & MacPhee, A. G. (2011). Proton radiography of laser-driven imploding target in cylindrical geometry. *Phys. Plasmas*, *18*, 012704.
42. Volpe, L., Batani, D., Baton, S., Pérez, F., Koenig, M., Nicolai, Ph., Vauzour, B., & Santos, J. J. (2011). Proton radiography for inertial confinement fusion. *J. Korean Phys. Soc.*, *59*, 3160–3165.
43. Rossi, B., & Greisen, K. (1941). Cosmic-ray theory. *Rev. Mod. Phys.*, *13*(4), 240.
44. Bethe, H. (1930). Zur Theorie des Durchgangs schneller Korpuskularstrahlen durch Materie [Theory of the passage of fast corpuscular rays through matter]. *Ann. Physik*, *397*(3), 325–400.
45. Fensin, M. L., Hendricks, J. S., & Anghaie, S. (2010). The enhancements and testing for the MCNPX 2.6.0 depletion capability. *Nucl. Technol.*, *170*(1), 68–79.